ADVANCED MATERIALS
www.advmat.de

Simultaneously Enhancing Exciton/Charge Transport in Organic Solar Cells by an Organoboron Additive

*Heng Lu, Kai Chen, Raja Sekhar Bobba, Jiangjian Shi, Mengyang Li, Yilin Wang, Jingwei Xue, Peiyao Xue, Xiaojian Zheng, Karen E. Thorn, Isabella Wagner, Chao-Yang Lin, Yin Song, Wei Ma, Zheng Tang, Qingbo Meng, Quinn Qiao, Justin M. Hodgkiss, and Xiaowei Zhan**

Efficient exciton diffusion and charge transport play a vital role in advancing the power conversion efficiency (PCE) of organic solar cells (OSCs). Here, a facile strategy is presented to simultaneously enhance exciton/charge transport of the widely studied PM6:Y6-based OSCs by employing highly emissive *trans*-bis(dimesitylboron)stilbene (BBS) as a solid additive. BBS transforms the emissive sites from a more H-type aggregate into a more J-type aggregate, which benefits the resonance energy transfer for PM6 exciton diffusion and energy transfer from PM6 to Y6. Transient gated photoluminescence spectroscopy measurements indicate that addition of BBS improves the exciton diffusion coefficient of PM6 and the dissociation of PM6 excitons in the PM6:Y6:BBS film. Transient absorption spectroscopy measurements confirm faster charge generation in PM6:Y6:BBS. Moreover, BBS helps improve Y6 crystallization, and current-sensing atomic force microscopy characterization reveals an improved charge-carrier diffusion length in PM6:Y6:BBS. Owing to the enhanced exciton diffusion, exciton dissociation, charge generation, and charge transport, as well as reduced charge recombination and energy loss, a higher PCE of 17.6% with simultaneously improved open-circuit voltage, short-circuit current density, and fill factor is achieved for the PM6:Y6:BBS devices compared to the devices without BBS (16.2%).

1. Introduction

Organic solar cells (OSCs) are promising as environmentally friendly power generators and have some merits such as flexibility, light weight, and semitransparency.[1] In recent years, the invention of fused-ring electron acceptors (FREAs),[2,3] represented by ITIC[4] and Y6,[5] promoted revolutionary development of the OSC field. Owing to the efforts on material design and device engineering, now power conversion efficiencies (PCEs) of the champion OSCs are in the range of 18–20%.[6–10] To achieve high efficiency in the OSCs, the photoactive layers should absorb sufficient photons to produce excitons and the photogenerated excitons must fast diffuse to the interface of donor and acceptor and efficiently dissociate into free charge carriers. The dynamic process of exciton diffusion is quite critical to the photoelectric conversion. Furthermore, charge-transport ability of the photovoltaic

H. Lu, P. Xue, X. Zheng, X. Zhan
School of Materials Science and Engineering
Peking University
Beijing 100871, China
E-mail: xwzhan@pku.edu.cn

K. Chen, K. E. Thorn, I. Wagner, J. M. Hodgkiss
MacDiarmid Institute for Advanced Materials and Nanotechnology
School of Chemical and Physical Sciences
Victoria University of Wellington
Wellington 6010, New Zealand

K. Chen, C.-Y. Lin
Robinson Research Institute
Faculty of Engineering
Victoria University of Wellington
Wellington 6010, New Zealand

R. S. Bobba, Q. Qiao
Department of Mechanical and Aerospace Engineering
Syracuse University
Syracuse, NY 13244, USA

J. Shi, Q. Meng
CAS Key Laboratory for Renewable Energy
Beijing Key Laboratory for New Energy Materials and Devices
Institute of Physics
Chinese Academy of Sciences
Beijing 100190, China

M. Li, Z. Tang
Center for Advanced Low-Dimension Materials
State Key Laboratory for Modification of Chemical
Fibers and Polymer Materials
College of Materials Science and Engineering
Donghua University
Shanghai 201620, China

Y. Wang, J. Xue, W. Ma
State Key Laboratory for Mechanical Behavior of Materials
Xi'an Jiaotong University
Xi'an 710049, China

Y. Song
School of Optics and Photonics
Beijing Institute of Technology
Beijing 100081, China

The ORCID identification number(s) for the author(s) of this article can be found under https://doi.org/10.1002/adma.202205926.

DOI: 10.1002/adma.202205926

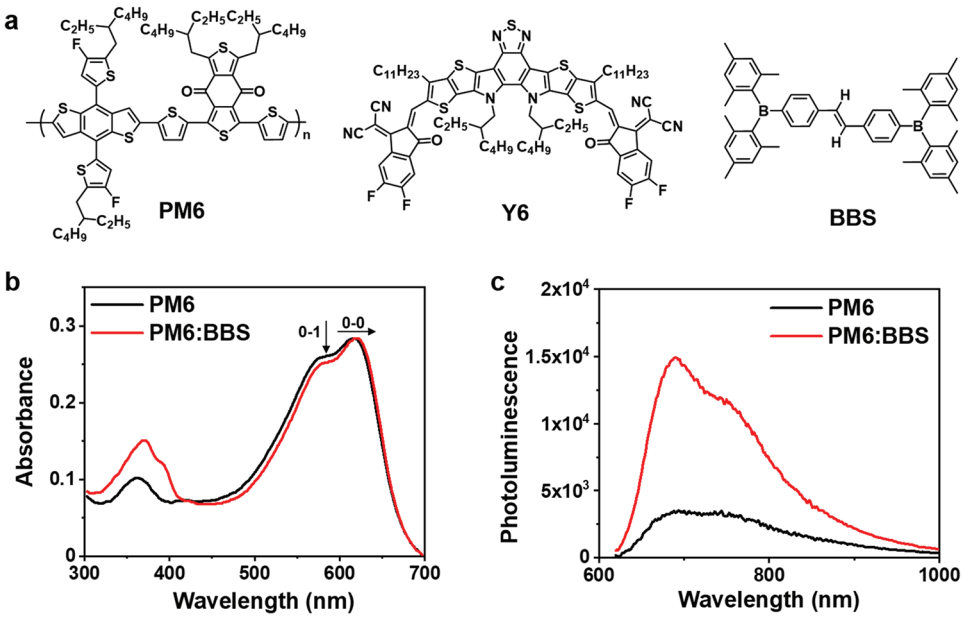

Figure 1. a) Chemical structures of PM6, Y6, and BBS. b) Absorption and c) PL spectra of PM6 and PM6:BBS (10:1, w/w) films.

materials is of great importance to ensure the free charge carriers are effectively collected by electrodes.

Generally, excitons generated directly by harvesting photons are singlet, which is governed by the electronic dipole transition process. Short diffusion length of singlet excitons, related to the diffusion coefficient and photoluminescence (PL) lifetime, limits further improvement of device efficiency. According to previous studies, the diffusion length of singlet excitons can be improved by optimizing molecular structure,[11] controlling molecular crystallinity,[12] and regulating density of exciton traps.[13] Delayed fluorescence materials, which have small energy gap and strong spin-orbit coupling between singlet and triplet state, were used to improve exciton diffusion length as a third component in efficient FREA-based OSCs.[14–16] Based on Förster energy transfer theory, exciton diffusion length and photoluminescence quantum yield (PLQY) have positive correlation,[17] accordingly exciton diffusion length can be increased through increasing PLQY.[18] For example, introduction of 9-fluorenone-1-carboxylic acid into the FREAs results in higher PLQY and longer lifetime of singlet excitons.[19]

At present, most active layers of high-performance OSCs consist of polymer donors and FREA acceptors. FREAs have shown excellent exciton diffusion behavior,[20–22] and their exciton diffusion coefficients are two orders of magnitude higher than those of fullerene acceptors.[20] The exciton diffusion lengths of polymer donors are generally inferior to those of the FREAs,[17,18,23] due to their relatively larger Stokes shifts and higher energetic disorder.[20] Therefore, increasing exciton diffusion lengths of the polymer donors is essential to further improve the device efficiency.

Here, we present a strategy of simultaneously enhancing exciton diffusion and charge transport in the OSCs by introducing a fluorescent organoboron derivative, *trans*-bis(dimesitylboron)stilbene[24] (BBS), into the representative PM6:Y6 system (**Figure 1**a). Triarylboranes are a class of widely used organic semiconductors with excellent emissive and electron-transport properties.[25,26] The addition of BBS leads to increased diffusion length of excitons, higher exciton dissociation probability, and faster charge generation. The charge-carrier transport properties of the active layers are also enhanced. An impressive PCE of 17.6% with a simultaneously improved V_{OC} of 0.858 V, J_{SC} of 27.1 mA cm^{-2}, and FF of 75.5% is achieved compared to the control device without BBS (PCE = 16.2%). Furthermore, with the addition of BBS, the PCEs of the devices based on the ITIC series acceptors are also improved.

2. Results and Discussion

2.1. Optoelectronic Properties

As shown in Figure S1, Supporting Information, the absorption spectra of PM6 and Y6 films are complementary covering 300–900 nm, while BBS shows an absorption band at 372 nm with a shoulder at 390 nm. After addition of BBS into the PM6 film (the weight ratio of BBS relative to PM6 is 0.1, unless indicated otherwise), the absorption band located at wavelengths shorter than 400 nm is substantially enhanced due to absorption overlapping of BBS and PM6 in this region (Figure 1b). The two films of PM6 and PM6:BBS exhibit same absorbance at their 0–0 transition peaks at ≈620 nm, and the 0–0 transition peak of the PM6:BBS film red shifts 5 nm relative to that of

X. Zhan
Key Laboratory of Eco-functional Polymer Materials
of Ministry of Education
College of Chemistry and Chemical Engineering
Northwest Normal University
Lanzhou 730070, China

the neat PM6 film. The PM6:BBS film shows a lower 0–1/0–0 intensity ratio than the PM6 film. The red shift of 0–0 transition peak and lower 0–1/0–0 intensity ratio of the PM6:BBS film suggest increased J-type aggregation of PM6 after the introduction of BBS.[27,28]

Figure 1c and Figure S2a, Supporting Information, show the PL spectra and normalized PL spectra of the PM6 films with and without BBS. The amount of PM6 keeps same in the two films, and the excitation wavelength is 600 nm. BBS would not be excited at 600 nm, and thus the emission in the PM6:BBS film is only from PM6. The PM6:BBS film shows a dominant PL peak at 690 nm (0–0 transition), the PL intensity is around five times larger than that of the neat PM6 film. The PLQY of the PM6:BBS film is 2.17%, a 50% increase relative to that of PM6 (1.42%). The more apparent 0–0 transition peak and higher PLQY of PM6:BBS further confirm increased J-type aggregation of PM6 with the addition of BBS.[29] Figure S2b–d, Supporting Information, shows the absorption, PL and normalized PL spectra of the Y6 films with and without BBS. BBS has less influence on Y6 compared with PM6.

The highest occupied molecular orbital (HOMO) energies of the materials are measured by ultraviolet photoemission spectroscopy (UPS, Figure S3, Supporting Information). The lowest unoccupied molecular orbital (LUMO) energies are calculated from their HOMO and optical bandgap (E_g, Figure S4a, Supporting Information). PM6 has a LUMO level of −3.56 eV and HOMO level of −5.37 eV, which match well with Y6 (−4.19 eV/−5.53 eV). The LUMO and HOMO levels of BBS are −2.75 eV and −5.75 eV, respectively.

2.2. Photovoltaic Properties

To investigate the photovoltaic properties, we fabricate OSCs with an architecture of ITO/PEDOT:PSS/active layer/PNDIT-F3N/Ag. For the active layer composed of PM6:Y6, the best D:A ratio is 1:1.2, and chloroform with 0.5% v/v 1-chloronaphthalene is used as the processing solvent. Different amount of BBS is added to PM6:Y6, and the optimized weight ratio of BBS:PM6 is 0.1. Table S1, Supporting Information, summarizes the best and average device characteristics with different amount of BBS under the illumination of an AM 1.5G solar simulator, 100 mW cm^{-2}. The champion device with BBS yields a higher PCE of 17.6% compared with the device without BBS (16.2%), with improvement of V_{OC} from 0.845 to 0.858 V, J_{SC} from 26.0 to 27.1 mA cm^{-2}, and FF from 73.7% to 75.5%. **Figure 2**a shows the representative current density–voltage (J–V) characteristics. Two more different active layers based on the ITIC series acceptors (Figure S4b, Supporting Information) are investigated to assess the effects of BBS (Table S2, Supporting Information). With the addition of BBS, PTB7-Th:FOIC and PM6:IDIC based devices show higher PCEs of 12.3% and 11.1%, respectively, compared to those without BBS (11.7% and 10.6%, respectively).

External quantum efficiency (EQE) spectra of devices with and without BBS are shown in Figure 2b. Photocurrent densities calculated by integrating the EQE curves are 26.9 and 25.8 mA cm^{-2} for the devices processed with and without BBS, respectively, which agree well with the J_{SC} values obtained from the J–V curves (within 1% mismatch). The absorption spectra of the active layers with different thickness are measured to calculate the internal quantum efficiency (IQE). From

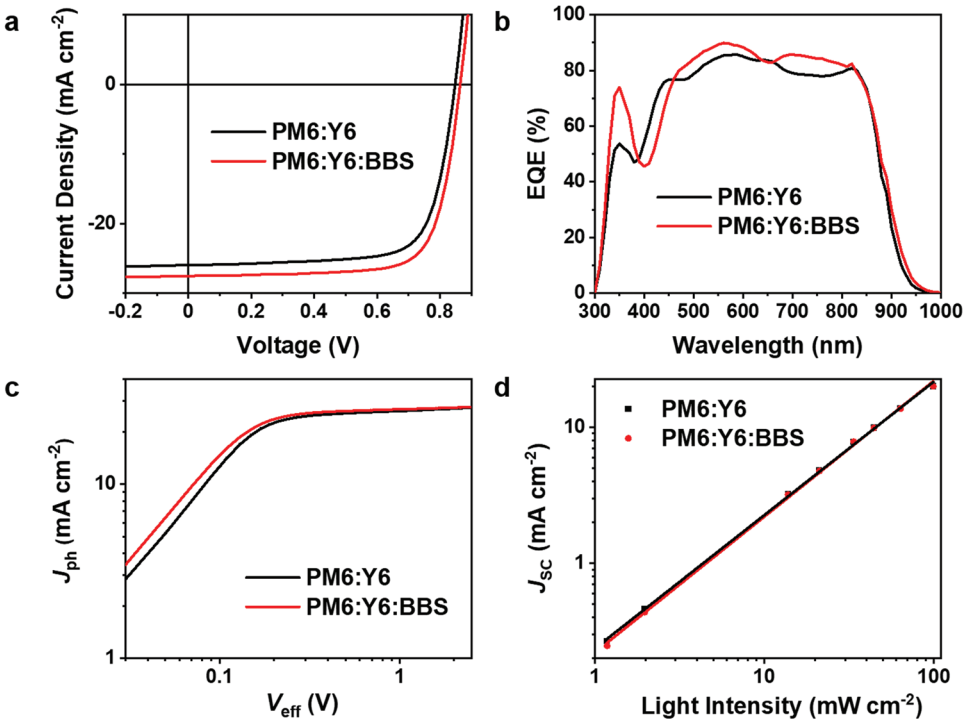

Figure 2. Characterization of the photovoltaic performance of optimized devices with and without BBS. a) J–V characteristics of solar cells measured under a simulated illumination of AM 1.5G (100 mW cm^{-2}). b) EQE curves. c) J_{ph} versus V_{eff}. d) J_{SC} versus light intensity.

the IQE curves displayed in Figure S5, Supporting Information, we note very high IQEs approaching 100% at 560 and 670 nm. Such high IQEs imply that essentially every absorbed photon can produce a separated pair of charge carriers and almost all photogenerated carriers are collected at the ITO and silver electrodes.

The photocurrent density (J_{ph}) versus effective voltage (V_{eff}) is measured to probe charge generation and extraction properties (Figure 2c). The saturated photocurrent density (J_{sat}) is obtained at high V_{eff} (>2.5 V), and the ratio of J_{SC} to J_{sat} represents the total efficiency of charge generation and extraction under short-circuit condition.[30] The J_{sat} of the devices with and without BBS are 27.9 and 27.7 mA cm^{-2}, and corresponding J_{SC}/J_{sat} values are 0.970 and 0.938, respectively, suggesting that the addition of BBS facilitates charge generation and extraction. We further measure J_{SC} as a function of light intensity (P_{light}), as shown in Figure 2d. The relationship of J_{SC} and P_{light} follows $J_{SC} \propto P_{light}^{\alpha}$, where α describes the degree of bimolecular recombination, and $\alpha = 1$ suggests no bimolecular recombination.[31] The α values are calculated to be 0.999 and 0.982 for devices with and without BBS, respectively, indicating that the addition of BBS can reduce bimolecular recombination.

Hole mobilities (μ_h) and electron mobilities (μ_e) of the blends are measured by space-charge-limited current (SCLC) method (Figure S6 and Table S3, Supporting Information). Electron-only device architecture is ITO/ZnO/active layer/Al, while hole-only devices use ITO/PEDOT:PSS/active layer/Au. The μ_h and μ_e of PM6:Y6 are 1.4×10^{-3} and 1.1×10^{-3} cm^2 V^{-1} s^{-1} (μ_h/μ_e = 1.3), respectively. With the addition of BBS, the μ_h and μ_e of the device simultaneously improve to 1.7×10^{-3} and 1.4×10^{-3} cm^2 V^{-1} s^{-1} (μ_h/μ_e = 1.2), respectively. Higher and more balanced charge mobilities are beneficial for higher J_{SC} and FF in PM6:Y6:BBS-based devices.[32]

2.3. Film Morphology

Grazing-incidence wide-angle X-ray scattering (GIWAXS) measurement is adopted to understand molecular packing behaviors in the active layers.[33] The 2D GIWAXS patterns and corresponding 1D profiles along out-of-plane (OOP) and in-plane (IP) directions of PM6:Y6, PM6:Y6:BBS, PM6 and Y6 films can be found in **Figure 3**a–e. The crystallization coherence length (CCL) is quantified using Scherrer equation. The calculated morphology parameters are summarized in Table S4, Supporting Information. The neat Y6 film shows obvious (100) and (001) diffraction peaks in IP direction and strong (010) peak in OOP direction, indicating sufficient π–π stacking and

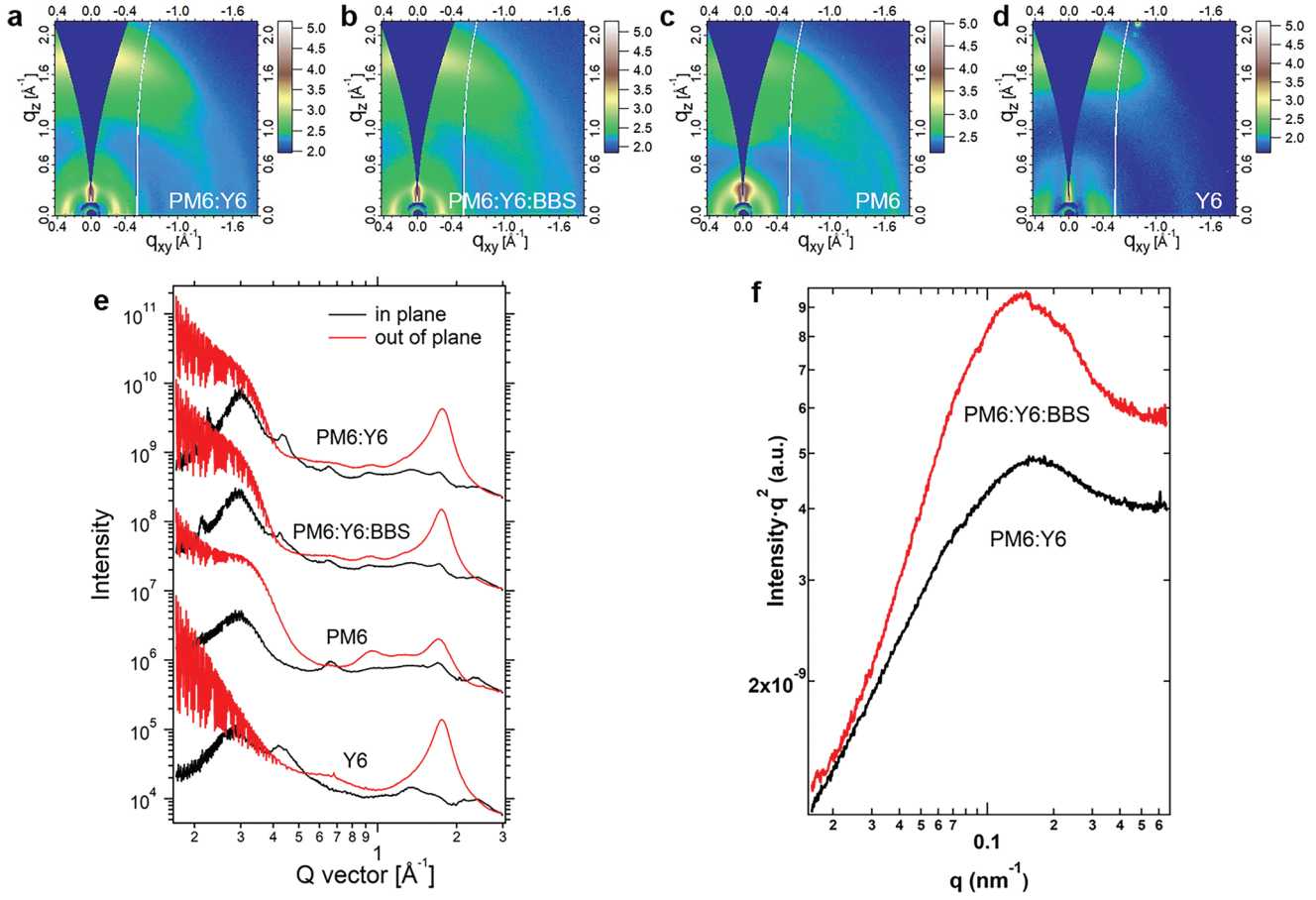

Figure 3. a–d) 2D GIWAXS patterns of PM6:Y6 (a), PM6:Y6:BBS (b), PM6 (c), and Y6 (d) films. e) The corresponding GIWAXS profiles along the out-of-plane and in-plane directions of the corresponding films. f) R-SoXS profiles in log scale of PM6:Y6 and PM6:Y6:BBS blend films.

a preferred face-on orientation, which is similar to the previous study.[5] The (001) diffraction peak (q = 0.42 Å^{-1}) is originated from the backbone ordering due to the end-group π–π stacking, which helps intermolecular electron transport. The blend PM6:Y6 and PM6:Y6:BBS films display a strong diffraction peak in the OOP direction at q = 1.75 Å^{-1}, associated with the π–π stacking of Y6. It is worth noting that the CCL of Y6 increases from 2.24 to 2.38 nm with the addition of BBS, confirming the stronger crystallization propensity, leading to increased electron mobility. The GIWAXS patterns and profiles of PM6:BBS and Y6:BBS films are also provided to verify the impact of BBS on the morphology of PM6 and Y6 (Figure S7, Tables S5 and S6, Supporting Information). The impact of BBS on morphology of PM6 and Y6 corresponds to that in blend films.

Resonant soft X-ray scattering (R-SoXS) is used to acquire the phase separation information of the active layers (Figure 3f).[34] The phase separation parameters are extracted and summarized in Table S7, Supporting Information. The PM6:Y6 and PM6:Y6:BBS films show scattering peaks at q = 0.17 and 0.15 nm^{-1}, respectively. The PM6:Y6:BBS film exhibits a larger domain size (21 nm) than the PM6:Y6 film (18 nm). Meanwhile, the relative phase purity of PM6:Y6:BBS (1.0) is higher than that of PM6:Y6 (0.8), which facilitates charge transport and reduces charge recombination.

2.4. Energy Loss

To figure out the origin for the difference of V_{OC} in devices with and without BBS, voltage loss (V_{loss}) is studied. The total voltage loss is related to three factors according to Equation (1)[35]

$$qV_{loss} = E_g - qV_{OC} = \left(E_g - qV_{OC,sq}\right) + \left(qV_{OC,sq} - qV_{OC,rad}\right) + q\Delta V_{OC,nr} = q\Delta V_1 + q\Delta V_2 + q\Delta V_3 \quad (1)$$

where q is the elementary charge, E_g is the bandgap of the blend, $V_{OC,sq}$ is the maximum voltage derived from the Shockley–Queisser theory, the EQE is assumed to be a step function, $V_{OC,rad}$ is the open-circuit voltage obtained when there is only radiative recombination loss in the device, and $\Delta V_{OC,nr}$ is the voltage loss due to non-radiative recombination, which can be determined by the measurement of electroluminescence external quantum efficiencies (EQE_{EL}) of the devices, according to Equation (2).[36]

$$\Delta V_{OC,nr} = \frac{kT}{q}\ln\left(EQE_{EL}^{-1}\right) \quad (2)$$

where k is the Boltzmann constant, T is absolute temperature in Kelvin.

First, to determine the $\Delta V_{OC,rad}$, electroluminescence (EL) spectra (Figure S8, Supporting Information) were measured. Then, using the reciprocal relation, the EL spectra were converted into EQE spectra, which were attached to the sensitive EQE (sEQE) spectra (**Figure 4**b), measured by a sensitive EQE setup. This allowed us to determine the radiative saturation current density ($J_{0,rad}$) using Equation (3).

$$J_{0,rad} = q\int_{-\infty}^{\infty} sEQE(E)\varnothing_{BB}(E)d(E) \quad (3)$$

where $\varnothing_{BB}(E)$ denotes the blackbody spectrum at 300 K. Subsequently, $V_{OC,rad}$ can be calculated using Equation (4).

$$V_{OC,rad} = \frac{kT}{q}\ln\left(\frac{J_{SC}}{J_{0,rad}}\right) \quad (4)$$

The detailed results are listed in Table S8, Supporting Information. In this work, the E_g of the blend films is determined from the absorption edge of neat acceptor (Y6), which is smaller than those of donor (PM6) and BBS in OSCs. Therefore, the $V_{OC,sq}$ could be obtained according to the Shockley–Queisser limit.[37] The ΔV_1 of two devices are both 0.262 V, while ΔV_2 of the device with BBS is smaller (0.083 V) than that of the control device without BBS (0.088 V). Furthermore, as shown in Figure 4a, EQE_{EL} of the device with BBS is higher (1.788×10^{-4}) than that of the control device without BBS (1.344×10^{-4}), giving rise to a smaller $\Delta V_{OC,nr}$ for the device with BBS (0.216 V vs 0.223 V). Note that the values of $\Delta V_{OC,nr}$ determined by the EQE_{EL} measurements agree well with those of ΔV_3, calculated using Equation (1). Thus, the V_{loss} of the device with BBS (0.549 V) is lower than that of the control device without BBS (0.562 V), which is the reason for the higher V_{OC} of BBS-based devices.

To assess the degree of energetic disorder, we calculate the Urbach energy (E_u) from the tail states of sEQE spectra,

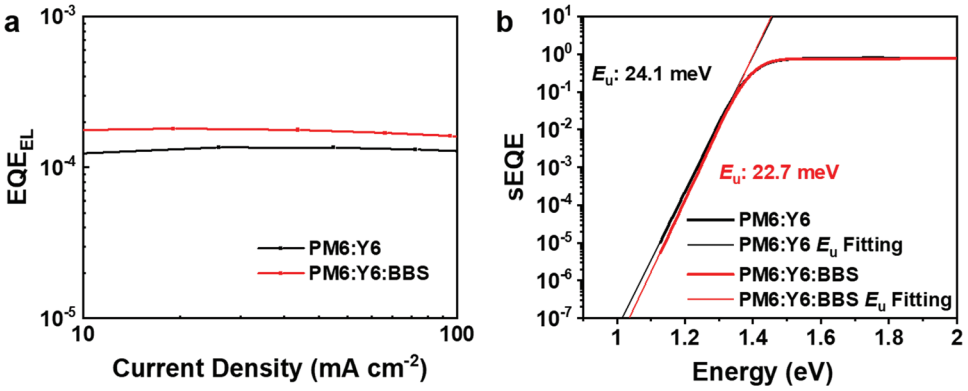

Figure 4. a) EQE_{EL} curves and b) sEQE spectra and E_u of PM6:Y6 and PM6:Y6:BBS.

according to $EQE(E) \propto \alpha_0 e^{(E-E_0)/E_u}$,[38] where α_0 and E_0 are constants, and E is the photon energy. Based on an exponential fit to the sub-bandgap sEQE, the blend with BBS exhibits a reduced energetic disorder with an E_u of 22.7 meV, while an E_u of 24.1 meV is observed in the PM6:Y6 blend (Figure 4b). The smaller energetic disorder, which is related to larger and purer domain in PM6:Y6:BBS film, can effectively reduce the $\Delta V_{OC,nr}$ in BBS-based cells.[39]

2.5. Modulated Transient Photocurrent/Photovoltage

Modulated transient photocurrent/photovoltage (TPC/TPV) methods are applied to further characterize the charge transport and recombination properties of these two cells.[40,41] As shown in **Figure 5**a, photocurrent of both cells exhibits fast rise and decay process in the timescale of 100–200 ns, mainly arising from the drift mechanism. The TPC curves also show tails in a longer timescale. The decay dynamics of the TPC tails of the cell based on PM6:Y6 ranging from 400 to 1000 ns is almost independent to the external bias voltage (i.e., internal electric field), while an obvious voltage-dependent behavior is observed for the cell based on PM6:Y6:BBS. These results mean that charge drift process is suppressed in the cell without BBS when the carrier density is reduced after charge extraction while charge transport in the cell with BBS is always dominated by the drift mechanism. This implies that the active layer in the cell without BBS has a more severe tail state distribution or molecular disordering, which is consistent with larger E_u of PM6:Y6. The charge trapping and detrapping process related to these tail states or the disordered charge hopping within the active layer limits the carrier drift and thus results in a diffusion-like charge-transport behavior. The slower charge transport and more severe charge trapping process will result in more charge loss during the charge-extraction process.

The influence of the charge trapping can also be reflected by the TPV results (Figure 5b). Positive external bias voltage (i.e., weakened internal electric field) can obviously decrease the TPV decay lifetime of the PM6:Y6-based cell, while the TPV decay lifetime of the cell based on PM6:Y6:BBS under bias voltages (e.g., 200–500 mV) is much longer than that of the cell without BBS. This further confirms that more charge trapping and recombination pathways exist in the active layer of the cell without BBS.

Another difference between these two cells lies in the voltage dependent TPC peak variation (Figure S9, Supporting Information). When weakening the internal electric field, the TPC peak of both cells decreases quasi-linearly, due to reduction in the charge drift velocity.[42] Under the same V_{eff}, the cell with BBS exhibits a much higher TPC peak than that without BBS, implying higher mobile charge concentration and higher exciton dissociation probability. Thus, the performance improvement of the PM6:Y6:BBS cell mainly arises from enhanced exciton dissociation and charge transport as well as reduced charge recombination in the charge generation and extraction process. The TPC/TPV results are in accord with the data of J_{sc}/J_{sat} and energy loss.

2.6. Photophysics

To investigate the photoexcitation dynamics, we apply the ultrafast techniques of transient gated photoluminescence (TGPL) spectroscopy and transient absorption (TA) spectroscopy. An excitation wavelength of 515 nm is used for all the ultrafast PL

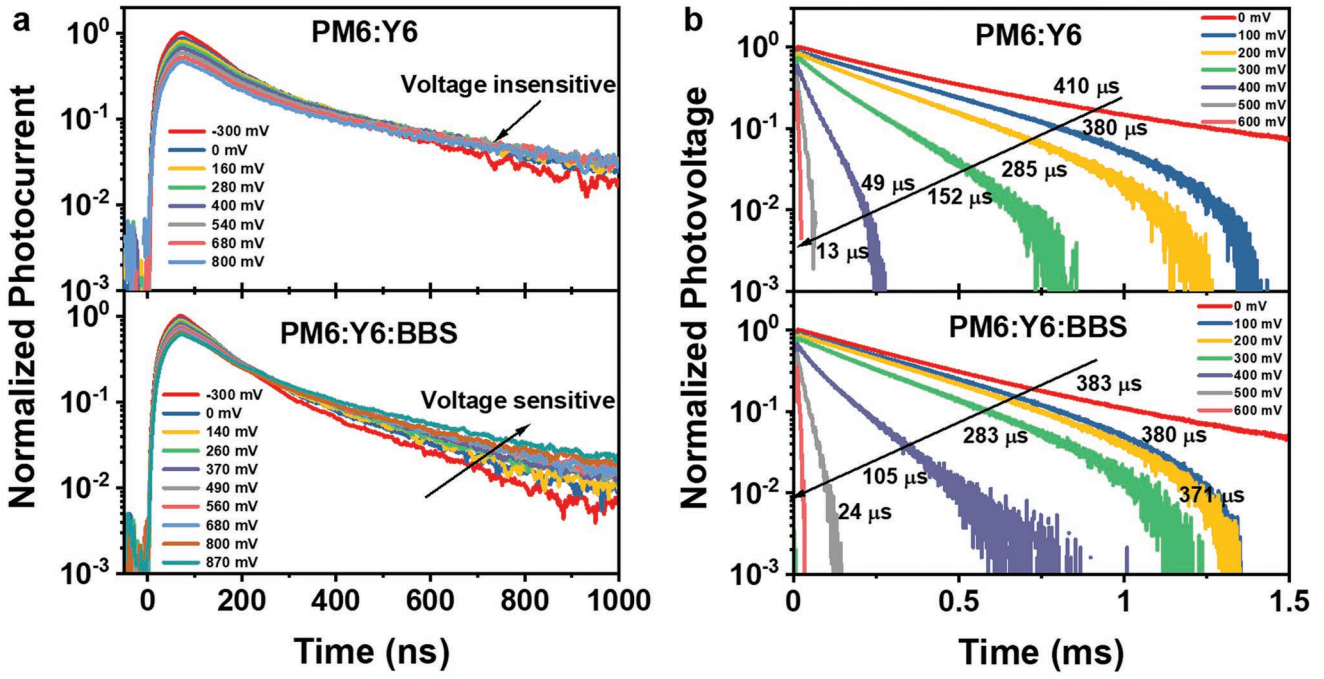

Figure 5. a) External bias voltage dependent transient photocurrent of the two cells in dark. b) External bias voltage dependent transient photovoltage of the two cells in dark. The TPV decay lifetime is extracted using an exponential fitting.

experiments. We first use TGPL to selectively probe the PM6 singlet exciton behavior of the PM6 and PM6:BBS thin films in the sub-picosecond to tens of picosecond (ps), the crucial time scale for the dissociation of PM6 exciton in the PM6:Y6 blend.[43] At a low excitation density of 2.5×10^{17} cm^{-3}, both PM6 and PM6:BBS thin films show similar emission dynamics with hundreds femtosecond (fs) decay (Figure S10, Supporting Information). These decay lifetimes are in line with previously reported ultrafast fluorescence upconversion measurements of PM6 in solution of ≈680 fs, with the faster decay being expected for the solid state material when comparing with the solution.[44] No observation of additional fast decay of the PM6:BBS sample suggests BBS does not introduce traps of singlet excitons.

Next, we compare fluence-dependent photoemission kinetics for the thin films of PM6 and PM6:BBS. From the experimental data, we can determine the bimolecular recombination rate of singlet excitons by exciton–exciton annihilation and thus obtain the exciton diffusion coefficient.[45,46] Global fitting is performed to fit the experimental data by Equation (5).

$$n(t) = \frac{n(0)e^{-kt}}{1 + \frac{\delta}{2k}n(0)\left[1 - e^{-kt}\right]} \quad (5)$$

where $n(t)$, $n(0)$, k, and δ are the excitation density as a function of time (cm^{-3}), initial excitation density at $t = 0$, monomolecular decay constant (s^{-1}) and bimolecular recombination rate (cm^3 s^{-1}), respectively. Fitting parameters are listed in Tables S9 and S10, Supporting Information.

Figure 6 shows the fluence dependent decays for PM6 and PM6:BBS thin films. We observe that the PM6 donor has no clear fluence dependence within the range of excitation densities under our experimental conditions. Our observation agrees with the same trend for the TA data within similar excitation density region in PM6 thin films.[18] Due to limitation of the ultrafast PL sensitivity, we cannot clearly resolve the fluence dependent kinetics to obtain exact δ value by global fitting. However, we can fit the data in Figure 6a with Equation (5) to get a range of δ from 4.5×10^{-7} to 6.4×10^{-7} cm^3 s^{-1}. In addition, the key message is lack of fluence dependence in PM6, which qualitatively suggests that the excitons are less mobile. Meanwhile, the fluence dependence in PM6:BBS shows a faster decay under higher excitation density, implying increase in exciton diffusion (Figure 6b). Comparing to neat PM6, we can determine a notably faster rate of $\delta = 2.4 \times 10^{-6}$ cm^3 s^{-1} for PM6:BBS. We calculate an exciton diffusion coefficient of $D = 0.18$ to 0.25 cm^2 s^{-1} for PM6 and $D = 0.96$ cm^2 s^{-1} for PM6:BBS, where $D = \delta/(8\pi r)$, and r is the annihilation radius approximated as 1 nm. The exciton diffusion coefficients here are higher than the values from previous TA measurement,[18] due to that PL selectively probes the highly mobile singlet excitons. We conclude that the addition of BBS significantly increases PM6 exciton diffusion and hence potentially improves the exciton dissociation in device.

To verify this point, we compare the PL emission of PM6 donor with PM6:Y6 and PM6:Y6:BBS blends (**Figure 7**a). We note first that the PM6:Y6 blend has a shorter lifetime (≈400 fs amplitude weighted half-life) than the neat PM6 (≈550 fs), while the PM6:Y6:BBS system has an even shorter lifetime (≈300 fs).

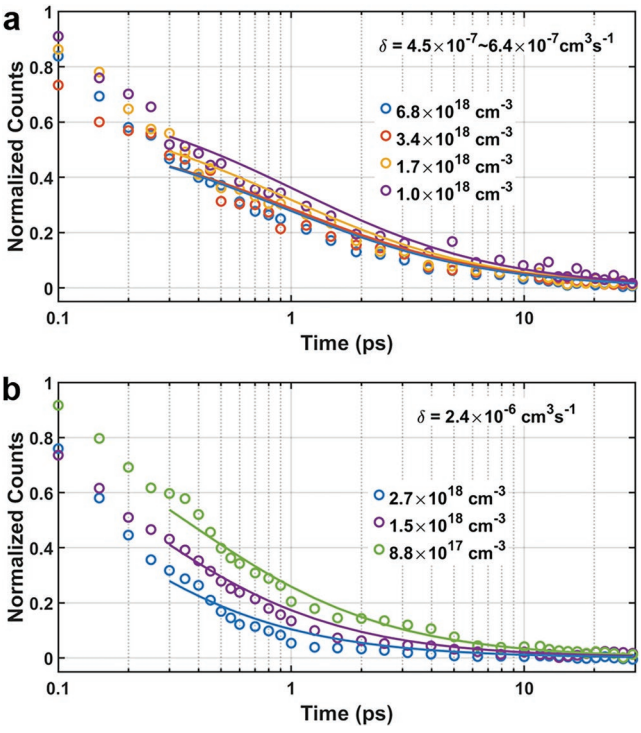

Figure 6. Fluence dependent PL decays and the fitting kinetics with Equation (5) for PM6 (a) and PM6:BBS (b) thin films.

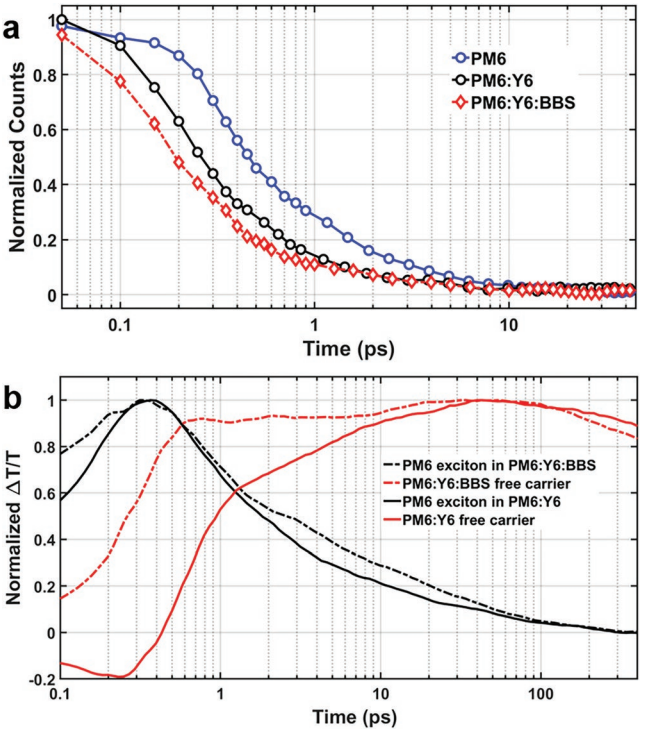

Figure 7. a) Kinetics of the integrated photo-emission of PM6 donor (blue circles), PM6:Y6 blend (black circles), and PM6:Y6:BBS blend (red diamonds) at pump fluence of 7 μJ cm^{-2}. b) Kinetics of the spectral components of the PM6 exciton (black) and charge carrier (red) for PM6:Y6 (solid line) and PM6:Y6:BBS (dash line) thin films, respectively.

The faster decay of the PM6 excitons in the PM6:Y6:BBS thin films indicates more efficient exciton dissociation via exciton diffusion and the energy transfer from PM6 to Y6,[18,47] which corresponds to the analysis of TPC peak variation. The enhancement of energy transfer is considered as the mechanism for boosting the efficiency of exciton diffusion and dissociation of PM6 exciton in the PM6:Y6:BBS thin films.

While the PL data shows the kinetics of singlet excitons in PM6, the TA data can probe the kinetics of free charge carriers. The TA spectral data can be analyzed using a Genetic Algorithm (GA) toolbox,[48] which extracts individual spectral component of excited species and their kinetics. In these experiments, an excitation pump wavelength of 620 nm is used so that we can perform and compare three TA experiments where Y6, PM6:Y6, and PM6:Y6:BBS all absorb the same wavelength. Figure S11, Supporting Information, shows the time-dependent TA spectra. We use a PM6 spectral time slice taken at early times (<1 ps) as the spectral feature of PM6 exciton, and a PM6:Y6 spectral time slice at late times (3.5 ns) as the spectral feature of free charge (Figure S12, Supporting Information). Applying these spectra to the PM6:Y6 and PM6:Y6:BBS blend spectra in the GA analysis reveals a third free component which is the Y6 exciton—this is confirmed in the spectral match with the neat Y6 TA experimental data.[49] Therefore, our spectral assignments are valid, and we can extract the kinetics of each excitation species. The analysis of such data is non-trivial as both PM6 and Y6 are excited at 620 nm making it difficult to strictly assign the spectral and kinetic signatures to either. Taking this into consideration, we can observe a faster charge generation in PM6:Y6:BBS (dashed red line in Figure 7b) compared to PM6:Y6 (solid red line). It is worth noting that the complicated spectral dynamics of the blend films may cause issue for applying multivariate curve resolution analysis in the sub-picosecond time scales. However, from the charge-carrier dynamic trends, the data still show more prompt charge generation in the PM6:Y6:BBS sample.

To investigate whether the addition of BBS influences hole-transfer dynamics at the interface, we perform TA under excitation at 850 nm. As shown in Figure S13, Supporting Information, we find that the time constants for hole transfer are 15 ps and 18 ps in the PM6:Y6 blend and the PM6:Y6:BBS blend, respectively, which are consistent with previous study.[43] The minor change in the hole-transfer dynamics in the two blends suggests that our strategy to improve the exciton diffusion and charge transport does not accompany with the cost of the charge-generation efficiency via the hole-transfer pathway.

From the TGPL and TA experimental data and the analysis presented above, we can conclude that the addition of BBS to both the PM6 donor and the PM6:Y6 blend aids the transport properties of PM6 excitons. This enhancement can be linked to the induced change of morphology. The morphology of conjugated polymers strongly affects their optical and electrical properties. Although the polymer thin films show complex morphology and microstructures, we can qualitatively use the simplified J- and H-aggregation model[27] to describe the effects of BBS. Compared with the neat PM6 thin films, the PM6:BBS shows more apparent 0–0 transition in the PL spectrum and higher PLQY, suggesting that BBS transforms the emissive sites from more H-aggregate into more J-aggregate. Therefore, the high fluorescence rate character of the modified J-aggregate like molecular packing can benefit the resonance energy transfer for PM6 exciton diffusion and energy transfer from PM6 to Y6. Interestingly, the macroscopic morphology of PM6 in PM6:Y6 and PM6:Y6:BBS films, showing π–π stacking features, appears to remain unchanged in GIWAXS characterization, while their photoluminescence originated from emissive microdomains differs significantly. Our observation suggests the formation of more emissive microdomains with the addition of BBS, where energy is funneled quickly to localized emissive states. This work provides a new means of morphology optimization, enhancing exciton diffusion by introducing local high emissive sites while maintaining the macroscopic π–π stacking to facilitate charge transport.[27,50]

2.7. Current-Sensing Atomic Force Microscopy (C-AFM)

C-AFM can be used to probe local charge-carrier dynamics in photoactive layers with improved spatial resolution, and also overcome the obstacles of normal atomic force microscopy (AFM) circuit bandwidth to detect the local characteristics with improved temporal resolution. Figure S14a,b, Supporting Information, shows 1 μm × 1 μm contact mode AFM topography of PM6:Y6 and PM6:Y6:BBS films, and Figure S14c,d, Supporting Information, shows their current-sensing AFM (C-AFM) images. The average currents for PM6:Y6 and PM6:Y6:BBS samples are 61 and 112 pA, respectively. As the C-AFM setup is made to selectively detect the electron current by using the inverted device architecture of the samples, and incorporating an electron-transport layer (ZnO) between the active layer and bottom ITO electrode, the more conductive region can be assigned as the acceptor-rich region, whereas the less conductive region can be assigned as the donor-rich region.[51,52] A 100 nm × 100 nm area shown by the red square includes both donor-rich and acceptor-rich regions on the topography image (Figure S14, Supporting Information). These 100 nm × 100 nm areas are used for mapping nanoscale charge dynamics.

Figure 8a,b presents the nanoscale charge-carrier recombination lifetime (τ_r) mapping of both PM6:Y6 and PM6:Y6:BBS samples indicated by red square. To compare charge-carrier dynamics between the samples, both donor-rich and acceptor-rich regions are shown by white dashed lines. A longer τ_r indicates improved charge-carrier lifetime. The mean charge-carrier lifetime (τ_r) is longer in BBS-based sample ($\tau_r = 4.94 \pm 0.39$ μs) than that of PM6:Y6 ($\tau_r = 4.70 \pm 0.31$ μs). Further examination of histograms (Figure S15a,b, Supporting Information) derived from mapping images reveals that the sample without BBS exhibits 86.6% of $\tau_r < 4.80$ μs, while the BBS-based sample has only 19.9% of $\tau_r < 4.80$ μs. The τ_r mapping and histogram indicate that the PM6:Y6:BBS sample has a longer recombination lifetime compared to the PM6:Y6 sample.

Figure 8c,d presents the nanoscale charge-carrier transport time (τ_t) mapping of both PM6:Y6 and PM6:Y6:BBS samples indicated by red square. A shorter τ_t indicates improved charge-carrier transport rate. The mean charge-carrier transport time is shorter in BBS-based sample ($\tau_t = 4.52 \pm 0.28$ μs) than that of PM6:Y6 ($\tau_t = 4.67 \pm 0.38$ μs). Further the examination of histograms (Figure S15c,d, Supporting Information) derived from mapping reveals that the sample without BBS has 11.8% of τ_t

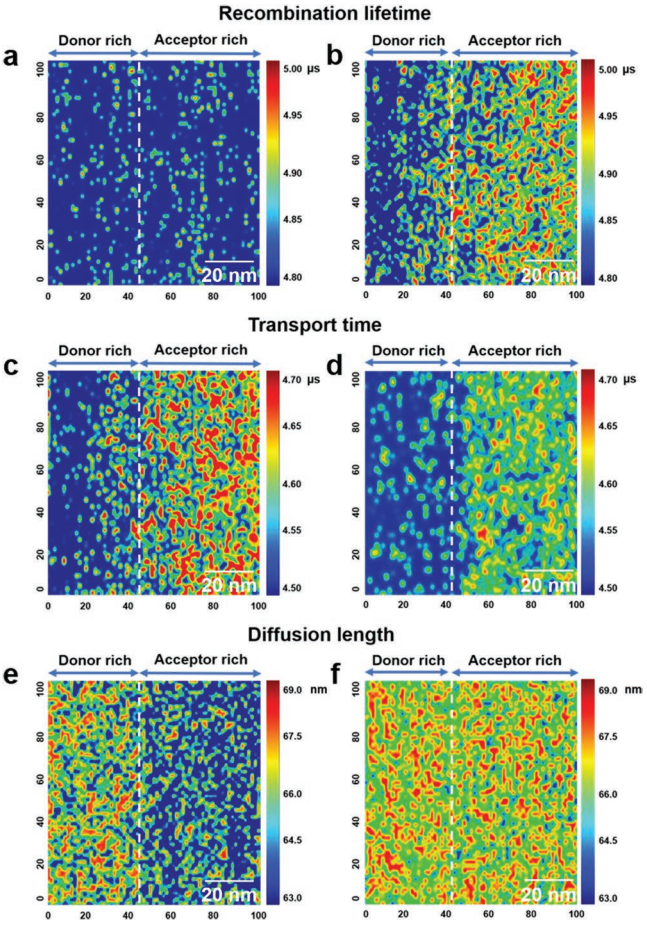

Figure 8. a–f) Nanoscale mapping of 100 nm × 100 nm red square regions (Figure S14, Supporting Information) of τ_r for PM6:Y6 (a) and PM6:Y6:BBS (b), τ_t for PM6:Y6 (c) and PM6:Y6:BBS (d), and L_D for PM6:Y6 (e) and PM6:Y6:BBS (f).

value >4.90 μs, while only 2.66% of τ_t > 4.90 μs in BBS-based sample. The τ_t mapping and histogram indicate that the PM6:Y6:BBS sample has a shorter charge-carrier transport time (τ_t) compared to the PM6:Y6 sample.

Finally, Figure 8e,f represents the nanoscale charge-carrier diffusion length (L_D) mapping of both PM6:Y6 and PM6:Y6:BBS samples indicated by red square. L_D is obtained by Equation (6)[53]

$$L_D = L \times \sqrt{\tau_r/(2.35 \times \tau_t)} \quad (6)$$

where L represents the active layer thickness. The mean charge-carrier diffusion length for the PM6:Y6:BBS sample is 68.2 ± 3.9 nm, which is longer than that of the PM6:Y6 sample (65.4 ± 3.1 nm). Further examination of histograms (Figure S15e,f, Supporting Information) derived from mapping reveals that the sample without BBS has only 15.9% of L_D value >67.5 nm, while 36.3% of L_D > 67.5 nm in BBS-based samples. The L_D mapping and histogram indicate that the addition of BBS can effectively increase the charge-carrier diffusion length of the active layer. This observation of enhanced local carrier-transport properties due to the decrease of trap-assisted recombination[54–56] well agrees with enhanced bulk charge mobilities and the conclusion of TPC and TPV, resulting in overall improved photovoltaic performance.

3. Conclusion

The PL intensity and quantum yield of PM6 significantly increase in the PM6:BBS (1:0.1) blend film, suggesting that BBS transforms the emissive sites from more H-type aggregate into more J-type aggregate. TGPL reveals a faster exciton diffusion rate for PM6:BBS than PM6. The faster decay of the PM6 excitons in the PM6:Y6:BBS films indicates more efficient exciton dissociation via exciton diffusion and energy transfer from PM6 to Y6. A faster charge generation in PM6:Y6:BBS compared to PM6:Y6 can also be observed from TA. BBS helps improve the π–π stacking of Y6 to show stronger crystallization propensity, accounting for the higher electron mobility. C-AFM demonstrates longer charge-carrier recombination lifetime, shorter charge-carrier transport time and thus improved charge-carrier diffusion length in PM6:Y6:BBS. The results of TPC and TPV manifest the performance improvement of the PM6:Y6:BBS device mainly arises from enhanced exciton dissociation and charge-transport ability, which agrees well with the conclusions of TGPL, TA, and C-AFM. Moreover, the nonradiative recombination is suppressed in devices by the addition of BBS due to the smaller energetic disorder, corresponding to the higher phase purity in PM6:Y6:BBS blend. With enhanced exciton diffusion, exciton dissociation, charge generation, and charge transport, as well as reduced charge recombination and energy loss, PM6:Y6:BBS based OSCs exhibit a higher PCE of 17.6% compared with that without BBS (16.2%), with simultaneous improvement of V_{OC}, J_{SC}, and FF. For OSCs based on other photoactive layers, including PTB7-Th:FOIC and PM6:IDIC, BBS is also able to enhance the device performance. This study provides a facile strategy of morphology optimization, increasing exciton diffusion by introducing local high emissive sites while maintaining the macroscopic π–π stacking to facilitate charge transport, and finally improving the performance of OSCs.

Supporting Information

Supporting Information is available from the Wiley Online Library or from the author.

Acknowledgements

X.Z. thanks the NSFC (Nos. U21A20101 and 21734001). J.M.H., K.C., and K.E.T. acknowledge financial support from the Marsden Fund of New Zealand. W.M. thanks the NSFC (21875182). X-ray data was acquired at beamlines 7.3.3 and 11.0.1.2 at the Advanced Light Source, which is supported by the Director, Office of Science, Office of Basic Energy Sciences, of the U.S. Department of Energy under Contract No. DE-AC02-05CH11231. The authors thank Chenhui Zhu at beamline 7.3.3 and Cheng Wang at beamline 11.0.1.2 for assistance with data acquisition. Q.Q. thanks Abiral Baniya and Sally Mabrouk for the characterization of C-AFM. Y.S. acknowledges support from the NSFC (No. 62105030). Y.S. also thanks Pengcheng Mao at the Analysis & Testing Center, Beijing Institute of Technology and Jiayu Wang, Prof. Yuxiang Weng at Institute of Physics, Chinese Academy of Sciences for their assistance with TA measurements.

Conflict of Interest

The authors declare no conflict of interest.

Data Availability Statement

The data that support the findings of this study are available from the corresponding author upon reasonable request.

Keywords

charge transport, exciton diffusion, fused-ring electron acceptors, organic solar cells, organoboron

Received: June 29, 2022
Revised: August 10, 2022
Published online: September 16, 2022

[1] F. C. Krebs, N. Espinosa, M. Hosel, R. R. Sondergaard, M. Jorgensen, *Adv. Mater.* **2014**, *26*, 29.
[2] J. Wang, P. Xue, Y. Jiang, Y. Huo, X. Zhan, *Nat. Rev. Chem.* **2022**, *6*, 614.
[3] C. Yan, S. Barlow, Z. Wang, H. Yan, A. K. Y. Jen, S. R. Marder, X. Zhan, *Nat. Rev. Mater.* **2018**, *3*, 18003.
[4] Y. Lin, J. Wang, Z. G. Zhang, H. Bai, Y. Li, D. Zhu, X. Zhan, *Adv. Mater.* **2015**, *27*, 1170.
[5] J. Yuan, Y. Zhang, L. Zhou, G. Zhang, H.-L. Yip, T.-K. Lau, X. Lu, C. Zhu, H. Peng, P. A. Johnson, M. Leclerc, Y. Cao, J. Ulanski, Y. Li, Y. Zou, *Joule* **2019**, *3*, 1140.
[6] C. Li, J. Zhou, J. Song, J. Xu, H. Zhang, X. Zhang, J. Guo, L. Zhu, D. Wei, G. Han, J. Min, Y. Zhang, Z. Xie, Y. Yi, H. Yan, F. Gao, F. Liu, Y. Sun, *Nat. Energy* **2021**, *6*, 605.
[7] G. Cai, Z. Chen, X. Xia, Y. Li, J. Wang, H. Liu, P. Sun, C. Li, R. Ma, Y. Zhou, W. Chi, J. Zhang, H. Zhu, J. Xu, H. Yan, X. Zhan, X. Lu, *Adv. Sci.* **2022**, *9*, 2200578.
[8] K. Chong, X. Xu, H. Meng, J. Xue, L. Yu, W. Ma, Q. Peng, *Adv. Mater.* **2022**, *34*, 2109516.
[9] L. Zhu, M. Zhang, J. Xu, C. Li, J. Yan, G. Zhou, W. Zhong, T. Hao, J. Song, X. Xue, Z. Zhou, R. Zeng, H. Zhu, C. C. Chen, R. C. I. MacKenzie, Y. Zou, J. Nelson, Y. Zhang, Y. Sun, F. Liu, *Nat. Mater.* **2022**, *21*, 656.
[10] Z. Zheng, J. Wang, P. Bi, J. Ren, Y. Wang, Y. Yang, X. Liu, S. Zhang, J. Hou, *Joule* **2022**, *6*, 171.
[11] S. B. Rim, R. F. Fink, J. C. Schoneboom, P. Erk, P. Peumans, *Appl. Phys. Lett.* **2007**, *91*, 173504.
[12] R. R. Lunt, J. B. Benziger, S. R. Forrest, *Adv. Mater.* **2010**, *22*, 1233.
[13] O. V. Mikhnenko, M. Kuik, J. Lin, N. van der Kaap, T. Q. Nguyen, P. W. Blom, *Adv. Mater.* **2014**, *26*, 1912.
[14] X. Du, Y. Yuan, L. Zhou, H. Lin, C. Zheng, J. Luo, Z. Chen, S. Tao, L. S. Liao, *Adv. Funct. Mater.* **2020**, *30*, 1909837.
[15] Z. Wang, R. F. Wang, Y. Mi, K. Lu, Y. A. Liu, C. Yang, J. Q. Zhang, X. F. Liu, Y. Wang, Z. G. Shuai, Z. X. Wei, *Chem. Mater.* **2021**, *33*, 4578.
[16] L. Y. Cao, X. Y. Du, H. Lin, C. J. Zheng, Z. H. Chen, S. L. Tao, *J. Mater. Chem. C* **2020**, *8*, 17429.
[17] O. V. Mikhnenko, P. W. M. Blom, T.-Q. Nguyen, *Energy Environ. Sci.* **2015**, *8*, 1867.
[18] S. Y. Park, S. Chandrabose, M. B. Price, H. S. Ryu, T. H. Lee, Y. S. Shin, Z. Wu, W. Lee, K. Chen, S. X. Dai, J. S. Zhu, P. Y. Xue, X. W. Zhan, H. Y. Woo, J. Y. Kim, J. M. Hodgkiss, *Nano Energy* **2021**, *84*, 105924.
[19] Q. Guo, Y. Liu, M. Liu, H. Zhang, X. Qian, J. Yang, J. Wang, W. Xue, Q. Zhao, X. Xu, W. Ma, Z. Tang, Y. Li, Z. Bo, *Adv. Mater.* **2020**, *32*, 2003164.
[20] S. Chandrabose, K. Chen, A. J. Barker, J. J. Sutton, S. K. K. Prasad, J. Zhu, J. Zhou, K. C. Gordon, Z. Xie, X. Zhan, J. M. Hodgkiss, *J. Am. Chem. Soc.* **2019**, *141*, 6922.
[21] Y. Firdaus, V. M. Le Corre, S. Karuthedath, W. Liu, A. Markina, W. Huang, S. Chattopadhyay, M. M. Nahid, M. I. Nugraha, Y. Lin, A. Seitkhan, A. Basu, W. Zhang, I. McCulloch, H. Ade, J. Labram, F. Laquai, D. Andrienko, L. J. A. Koster, T. D. Anthopoulos, *Nat. Commun.* **2020**, *11*, 5220.
[22] J. Zhou, X. Wen, N. Tang, X. Zhou, C. Wang, N. Zheng, L. Liu, Z. Xie, *J. Phys. Chem. Lett.* **2020**, *11*, 7908.
[23] O. V. Mikhnenko, H. Azimi, M. Scharber, M. Morana, P. W. M. Blom, M. A. Loi, *Energy Environ. Sci.* **2012**, *5*, 6960.
[24] Z.-Q. Liu, Q. Fang, D.-X. Cao, D. Wang, G.-B. Xu, *Org. Lett.* **2004**, *6*, 2933.
[25] Z. M. Hudson, S. Wang, *Acc. Chem. Res.* **2009**, *42*, 1584.
[26] K. Suzuki, S. Kubo, K. Shizu, T. Fukushima, A. Wakamiya, Y. Murata, C. Adachi, H. Kaji, *Angew. Chem., Int. Ed.* **2015**, *54*, 15231.
[27] Y. Liu, K. Zhou, X. Zhou, W. Xue, Z. Bi, H. Wu, Z. Ma, W. Ma, *Macromol. Rapid Commun.* **2022**, 2100871.
[28] P. Urbánek, I. Kuřitka, J. Ševčík, J. Toušková, J. Toušek, V. Nádaždy, P. Nádaždy, K. Végsö, P. Šiffalovič, R. Rutsch, M. Urbánek, *Polymer* **2019**, *169*, 243.
[29] Y. Liu, Y. Guo, Y. Liu, *Small Struct.* **2020**, *2*, 2000083.
[30] V. D. Mihailetchi, L. J. Koster, J. C. Hummelen, P. W. Blom, *Phys. Rev. Lett.* **2004**, *93*, 216601.
[31] I. Riedel, J. Parisi, V. Dyakonov, L. Lutsen, D. Vanderzande, J. C. Hummelen, *Adv. Funct. Mater.* **2004**, *14*, 38.
[32] D. Bartesaghi, C. Perez Idel, J. Kniepert, S. Roland, M. Turbiez, D. Neher, L. J. Koster, *Nat. Commun.* **2015**, *6*, 7083.
[33] Y. L. Wang, X. H. Wang, B. J. Lin, Z. Z. Bi, X. B. Zhou, H. B. Naveed, K. Zhou, H. P. Yan, Z. Tang, W. Ma, *Adv. Energy Mater.* **2020**, *10*, 2000826.
[34] B. Lin, X. Zhou, H. Zhao, J. Yuan, K. Zhou, K. Chen, H. Wu, R. Guo, M. A. Scheel, A. Chumakov, S. V. Roth, Y. Mao, L. Wang, Z. Tang, P. Müller-Buschbaum, W. Ma, *Energy Environ. Sci.* **2020**, *13*, 2467.
[35] U. Rau, B. Blank, T. C. M. Muller, T. Kirchartz, *Phys. Rev. Appl.* **2017**, *7*, 044016.
[36] U. Rau, *Phys. Rev. B* **2007**, *76*, 085303.
[37] J. Liu, S. S. Chen, D. P. Qian, B. Gautam, G. F. Yang, J. B. Zhao, J. Bergqvist, F. L. Zhang, W. Ma, H. Ade, O. Inganas, K. Gundogdu, F. Gao, H. Yan, *Nat. Energy* **2016**, *1*, 16089.
[38] F. Urbach, *Phys. Rev.* **1953**, *92*, 1324.
[39] S. Liu, J. Yuan, W. Deng, M. Luo, Y. Xie, Q. Liang, Y. Zou, Z. He, H. Wu, Y. Cao, *Nat. Photonics* **2020**, *14*, 300.
[40] J. Shi, D. Li, Y. Luo, H. Wu, Q. Meng, *Rev. Sci. Instrum.* **2016**, *87*, 123107.
[41] J. Shi, Y. Li, Y. Li, D. Li, Y. Luo, H. Wu, Q. Meng, *Joule* **2018**, *2*, 879.
[42] J. Seifter, Y. Sun, H. Choi, B. H. Lee, T. L. Nguyen, H. Y. Woo, A. J. Heeger, *Adv. Mater.* **2015**, *27*, 4989.
[43] R. Wang, C. Zhang, Q. Li, Z. Zhang, X. Wang, M. Xiao, *J. Am. Chem. Soc.* **2020**, *142*, 12751.
[44] H. W. Nho, W. W. Park, B. Lee, S. Kim, C. Yang, O. H. Kwon, *Phys. Chem. Chem. Phys.* **2022**, *24*, 1982.
[45] P. E. Shaw, A. Ruseckas, I. D. W. Samuel, *Adv. Mater.* **2008**, *20*, 3516.
[46] Y. Tamai, H. Ohkita, H. Benten, S. Ito, *J. Phys. Chem. Lett.* **2015**, *6*, 3417.
[47] S. Karuthedath, J. Gorenflot, Y. Firdaus, N. Chaturvedi, C. S. P. De Castro, G. T. Harrison, J. I. Khan, A. Markina, A. H. Balawi, T. A. D. Pena, W. Liu, R. Z. Liang, A. Sharma, S. H. K. Paleti, W. Zhang, Y. Lin, E. Alarousu, S. Lopatin,

D. H. Anjum, P. M. Beaujuge, S. De Wolf, I. McCulloch, T. D. Anthopoulos, D. Baran, D. Andrienko, F. Laquai, *Nat. Mater.* **2021**, *20*, 378.
[48] Y. Vaynzof, A. A. Bakulin, S. Gelinas, R. H. Friend, *Phys. Rev. Lett.* **2012**, *108*, 246605.
[49] X. Zou, G. Wen, R. Hu, G. Dong, C. Zhang, W. Zhang, H. Huang, W. Dang, *Molecules* **2020**, *25*, 4118.
[50] P. W. Bohn, *Annu. Rev. Phys. Chem.* **1993**, *44*, 37.
[51] Y. Wu, S. Schneider, C. Walter, A. H. Chowdhury, B. Bahrami, H. C. Wu, Q. Qiao, M. F. Toney, Z. Bao, *J. Am. Chem. Soc.* **2020**, *142*, 392.
[52] M. Osaka, D. Mori, H. Benten, H. Ogawa, H. Ohkita, S. Ito, *ACS Appl. Mater. Interfaces* **2017**, *9*, 15615.
[53] A. B. Martinson, M. S. Goes, F. Fabregat-Santiago, J. Bisquert, M. J. Pellin, J. T. Hupp, *J. Phys. Chem. A* **2009**, *113*, 4015.
[54] S. Zeiske, O. J. Sandberg, N. Zarrabi, W. Li, P. Meredith, A. Armin, *Nat. Commun.* **2021**, *12*, 3603.
[55] Z. H. Chen, T. Wang, Z. C. Wen, P. Lu, W. Qin, H. Yin, X. T. Hao, *ACS Energy Lett.* **2021**, *6*, 3203.
[56] K. N. Zhang, X. Y. Du, Z. H. Chen, T. Wang, Z. Q. Yang, H. Yin, Y. Yang, W. Qin, X. T. Hao, *Adv. Energy Mater.* **2022**, *12*, 2103371.